Double-Sided Junctions Enable High-Performance Colloidal-Quantum-Dot Photovoltaics

Mengxia Liu, F. Pelayo García de Arquer, Yiying Li, Xinzheng Lan, Gi-Hwan Kim, Oleksandr Voznyy, Lethy Krishnan Jagadamma, Abdullah Saud Abbas, Sjoerd Hoogland, Zhenghong Lu, Jin Young Kim, Aram Amassian, and Edward H. Sargent*

Colloidal quantum dots (CQDs) are attractive materials for low-cost, large-scale optoelectronic devices such as light-emitting diodes,[1–3] photodetectors,[4,5] transistors,[6,7] and solar cells.[8–12] Their size-tunable bandgap[13,14] provides compelling properties in both light emission and solar harvesting applications.[15,16] Their processing from the solution phase paves the way for large-area manufacture and compatibility with physically flexible devices.

Major improvements to CQD photovoltaic performance have been achieved through device architecture engineering,[9,10,17] surface chemistry programming,[8,18] and structured electrodes for improved carrier collection.[11,19] Significant advances in CQD surface passivation have helped increase performance to certified power conversion efficiencies (PCEs) recently reaching 9.9%.[12,20]

To date, the most efficient CQD solar cells are based on the depleted heterojunction architecture.[12] In this strategy, the CQD solid is depleted of free carriers via a rectifying junction that ensures an appreciable built-in field across the thickness of the active layer. This facilitates carrier separation and extraction, reducing reliance on the as-yet incompletely efficient minority carrier diffusion process in CQD solids.[21] The needed low doping of the CQD solid has been achieved by progressive engineering of nanoparticle surfaces.

Impressive progress has been seen during the last years in increasing the CQD diffusion length (L_d), with reported values now exceeding 200 nm.[18] Nevertheless, since the absorption length in CQD solids is closer to 1 µm near the bandedge, continued improvements in charge extraction via the retention of a maximum of depletion, ideally at maximum power point (MPP) conditions, will further benefit performance.

In light of much recent progress made in the CQD solids, we took the view that it would be attractive to revisit the engineering of the electron-accepting electrode in the depleted heterojunction. This is particularly timely now that iodide-treated CQD solids, which are known to have a deepened band structure (bandedge and work function farther below vacuum) compared to prior organic-crosslinked CQD solids, are the basis of the best present-day CQD solids for photovoltaics.[9]

In ideal graded heterojunction architectures (n-i-p structure), two junctions should be obtained at both electrode/CQDs and i-/p-CQDs interfaces. However, due to the strong n-type behavior of the iodide-treated dots, very little band-bending is retained, at MPP, at the junction between the n-type electrode (normally ZnO/TiO₂) and the CQD active layer. What remains is the junction between the n- and p-type CQD solids. This fact contributes to increased recombination at MPP due to the loss of depletion.

Here we re-engineer the ZnO electrode to build a double-sided junction, i.e., one that includes not only a rectifying nCQD:pCQD junction in the quantum dot solid but also a strongly n+:n junction at the ZnO:nCQD interface.

We achieve this by incorporating In^{3+} into ZnO, which allows us to simultaneously adjust its band structure and carrier concentration, ultimately benefiting CQD PV performance. When the optimal doping density and electron affinity are achieved, the degenerately doped electrode forms a rectifying junction with the n-type CQD layer, and this increases the total depleted thickness within the CQD solid.

Most strikingly, the benefits are felt even at the MPP: the presence of electric fields at both electron and hole collecting layer interfaces (i.e., the fact of having double-sided junctions) considerably improves charge collection and, consequently, fill factor (FF). This, together with the increased V_{oc} due to a higher built-in potential and an improved short-circuit current density (J_{sc}) that now reaches 24 mA cm^{-2}, enables us to obtain herein the highest CQD photovoltaic solar power conversion efficiency (PCE = 10.8%) reported to date.

The prototypical device architecture of the best-performing CQD solar cells is shown in **Figure 1**a. The photoactive CQD solid is deposited on a ZnO electrode (≈40 nm thick) atop indium doped tin oxide (ITO) using a layer-by-layer procedure. CQD films consist of eight layers of tetrabutylammonium iodide (TBAI) solid-state exchanged CQDs followed by two

M. Liu, Dr. F. P. García de Arquer, Dr. X. Lan,
Dr. G.-H. Kim, Dr. O. Voznyy, A. S. Abbas,
Dr. S. Hoogland, Prof. E. H. Sargent
Department of Electrical and Computer Engineering
University of Toronto
10 King's College Road, Toronto, Ontario, M5S 3G4, Canada
E-mail: ted.sargent@utoronto.ca
Y. Li, Prof. Z. Lu
Department of Materials Science and Engineering
University of Toronto
184 College Street, Toronto, Ontario, M5S 3E4, Canada
Dr. G.-H. Kim, Prof. J. Y. Kim
School of Energy and Chemical Engineering
Ulsan National Institute of Science and Technology (UNIST)
Ulsan 689-798, South Korea
L. K. Jagadamma, Prof. A. Amassian
King Abdullah University of Science and Technology (KAUST)
Solar and Photovoltaic Engineering Research Center (SPERC)
and Physical Sciences and Engineering Division
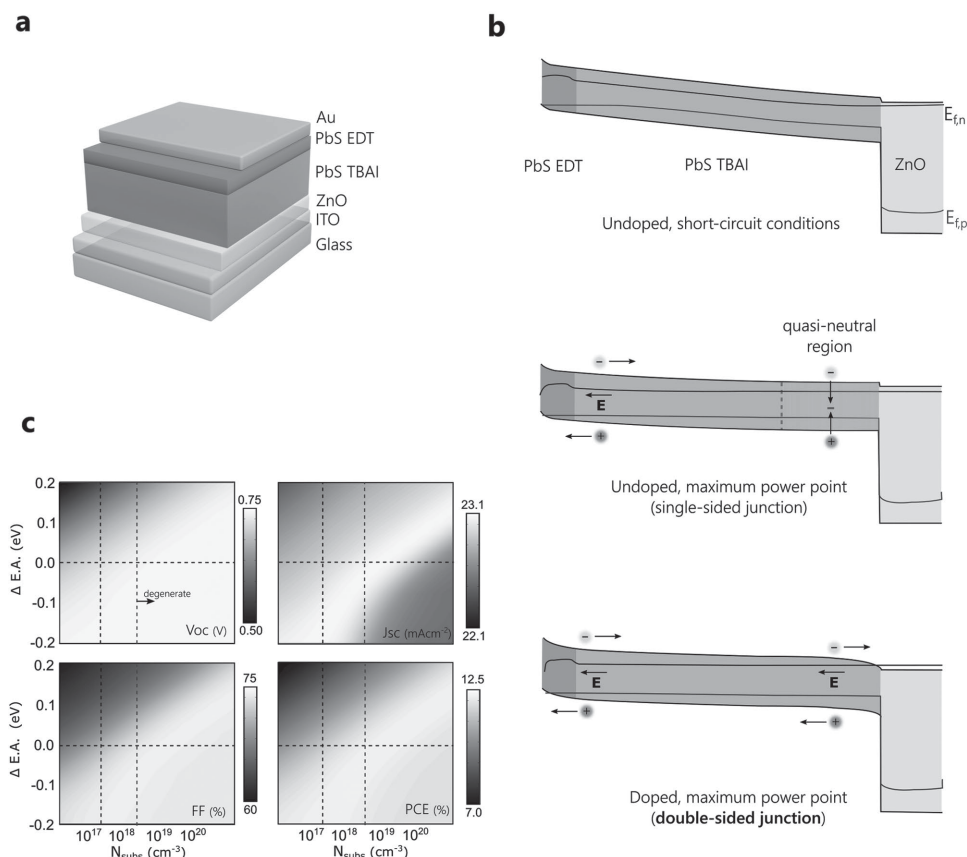4700 KAUST, Thuwal 23955-6900, Saudi Arabia

Figure 1. Double-sided junctions enable high performance colloidal quantum dot photovoltaics. a) Device architecture of a prototypical record CQD solar cell. b) Energy landscape after alignment of standard solar cells at short-circuit conditions (top), maximum power point (middle), as well as the corresponding super depleted sceneration for highly doped ZnO substrates. c) Photovoltaic figures of merit as a function of ZnO carrier concentration and valence-band energy shift. The intersection of black-dashed lines corresponds to the case of pristine ZnO. The vertical dashed line to the right in each of the plots denotes the limit or degenerated doping, over which excess electrons start filling the conduction band provoking an effective increase in the optical bandgap.

layers of 1,2-ethanedithiol (EDT) treatment. Prior to solid-state exchange, CQDs are subjected to a solution-phase passivation procedure that leverages iodine molecules and ultimately produces an extended diffusion length.[12] A gold electrode is deposited on top to collect photogenerated holes.

As seen in the energy band diagram at short-circuit conditions (Figure 1b), when the materials are brought together, a uniform electric field in the CQD active layer assists in the separation and extraction of photocarriers via the drift mechanism. However, at MPP, a considerable fraction of the film is not depleted due to a lack of rectifying junction at electron-collecting interface. Instead, a quasi-neutral region is established in which charge carrier collection increasingly relies on diffusion. Since CQD solids are not yet optimized for long-distance (multihundreds-of-nm) minority carrier diffusion,[22] recombination increases at the MPP.

We predicted that further increasing the net doping in the ZnO could form an added junction at this interface that would aid in keeping more full depletion of the CQD film even at the MPP condition (Figure 1b, bottom panel). The majority of the photogenerated carriers could then be collected by double-sided junctions before they recombine, resulting in an increased fill factor and overall device performance.

From simulations, when the carrier density in the ZnO electrode is dramatically increased from the conventional 10^{17} cm^{-3} level to an optimized mid-10^{19} cm^{-3} range, V_{oc} can increase from 0.68 to 0.71 V, while simultaneously increasing the fill factor from 0.69 to 0.74. In principle, this has the potential to increase the overall PCE of devices considerably from their 9.9%[12] starting point previously reported when optimal doping density and electron affinity are achieved. We note that judicious engineering of the electron affinity of the ZnO relative to the CQD solid is also desired for full optimization (Figure 1c).

We sought to utilize indium doping to increase the free carrier density in the ZnO. Indium is known to replace Zn, and this is expected to increase free carrier density without distorting the lattice (comparable atomic radius and ionic radius: indium ≈155 pm/81 pm vs zinc ≈135 pm/74 pm), and indium's 3^{+} oxidation state is expected to contribute strong n-doping of the ZnO.[23,24]

We prepared a systematic series of In:ZnO sol–gels on ITO (Experimental Section). The film thickness is 40 ± 5 nm and the surface roughness is 2.4 nm root mean square (RMS) (see Figure S1, Supporting Information). The amount of indium dopant is quantified by the atomic percentage of indium chloride used for sol–gel synthesis (0–5 at%). The successful incorporation of indium into ZnO was confirmed using X-ray
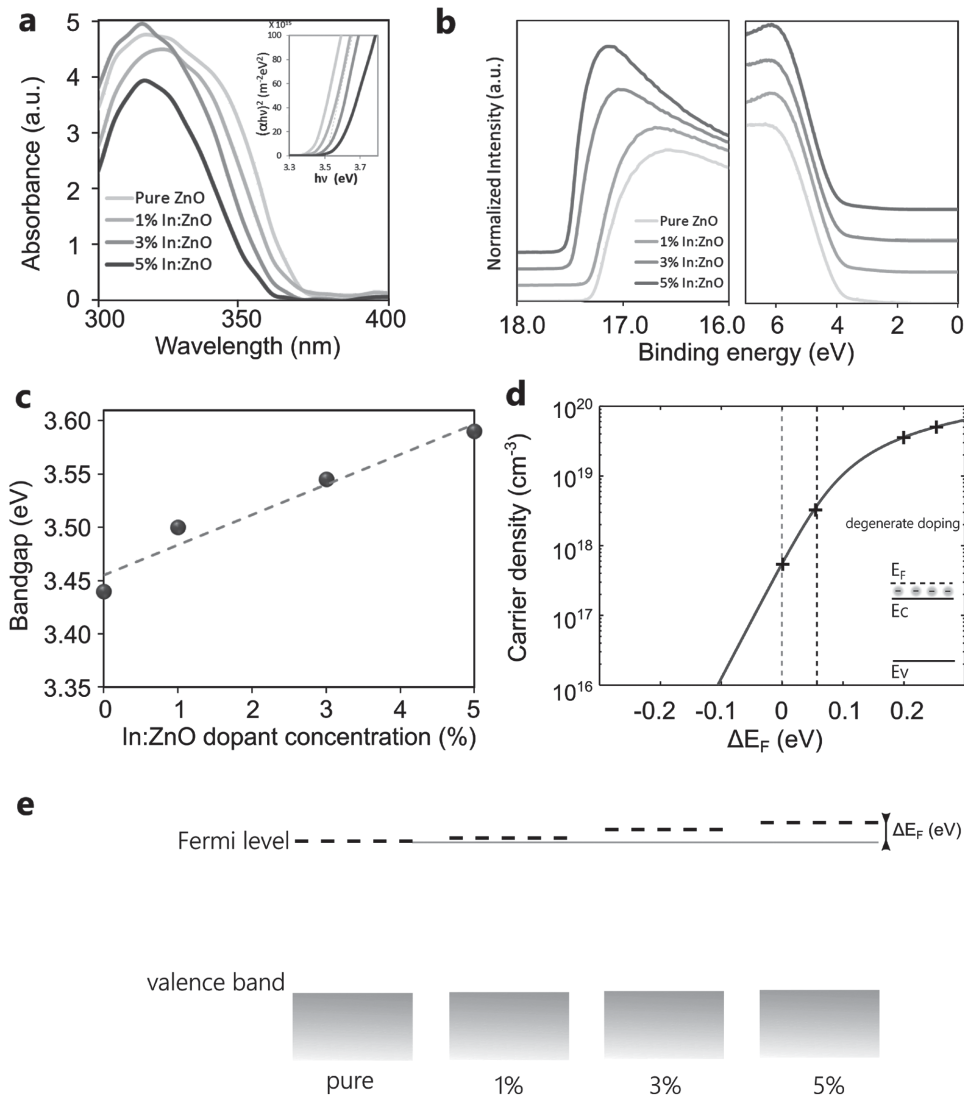
Figure 2. Optical and electronic properties of In-doped ZnO. a) Absorbance of pure and doped ZnO films with Tauc plots inset. b) UPS spectra of pure and In-doped ZnO. Work function decreases gradually as the dopant concentration increases, while valence-band position remains almost unchanged. c) Bandgap calculated from Tauc plots versus indium concentration in sol–gel. The bandgap is widened gradually as the dopant concentration increases. d) Carrier density as a function of Fermi level shift (ΔE_F). Up to a two orders of magnitude increase is observed for 5% In:ZnO. Crosses represent the points based on UPS and bandgap calculations. e) Estimated band structure of pure and doped ZnO.

photoemission spectroscopy (XPS) (Figure S2, Supporting Information). From the detected species, the 1 at% In:ZnO in-synthesis resulted in a $Zn_{0.99}In_{0.01}O$ final element composition, confirming the efficient incorporation of In.

We then proceeded to characterize the optoelectronic properties of the In:ZnO films. The optical absorption spectra for the cases of a number of distinct In doping levels are shown in **Figure 2**a. As the doping concentration increases, a blue-shift in the absorption edge is observed, and the bandgap widening is summarized in the Tauc plots of Figure 2a, inset. The widening of the gap is a signature of excess electrons filling the states above the conduction-band edge (the Burstein–Moss effect).[25] UV photoelectron spectroscopy (UPS) (Figure 2b) indicates that the valence-band maximum (VBM) level does not substantially change upon In introduction, whereas the work function continuously decreases,

a signature of n-type doping (see **Table 1**). The same finding is also confirmed using Kelvin-Probe Force microscopy measurements (Figure S3, Supporting Information).

Table 1. Valence-band maximum (VBM) level and Fermi level for pure and doped ZnO substrates relative to the vacuum. The Fermi level and VBM value are derived from UPS measurements. The Fermi level shifts are all relative to that of pure ZnO substrate.

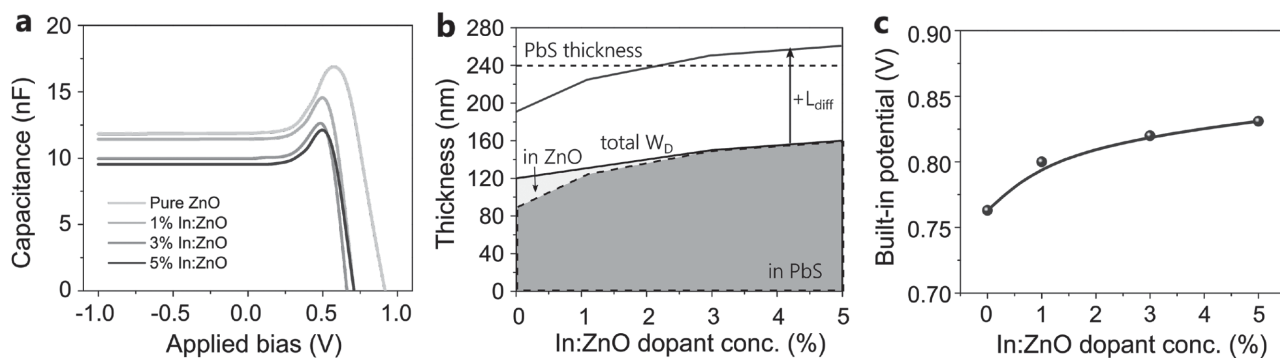|	VBM [eV]	Fermi level [eV]	Fermi level shift [eV]
Pure ZnO	−7.66	−3.93	0
1% In:ZnO	−7.66	−3.88	0.05
3% In:ZnO	−7.56	−3.73	0.20
5% In:ZnO	−7.55	−3.69	0.24

Figure 3. Increased depletion width and built-in potential. a) Capacitance–voltage traces of photovoltaic devices fabricated with different In:ZnO doped electrodes. By gradually increasing dopant concentration, the capacitance decreases illustrating the more depleted nature of the CQD film. b) Total depletion width (W_D) at maximum power point conditions, and its contribution to the different layers for different dopant concentrations. The combination of depletion and diffusion (L_d) suffices to overcome CQD thickness for In doping concentrations above 2%. c) Built-in voltage potential (V_{bi}) as a function of indium doping concentration.

The measured free carrier density (see Figure 2d and the Experimental Section) gradually increases from $n \approx 4 \times 10^{17}$ cm^{-3} to 5×10^{19} cm^{-3} for the highest In concentration (5%). Degenerate doping[26] is observed for concentrations above 3%, where the calculated carrier density surpasses the ZnO density of states at the conduction band (2×10^{19} cm$^{-3} > 4 \times 10^{18}$ cm^{-3}). At this point, the Fermi level shifts into the conduction band as excess electrons are incorporated, which correlates well with the bandgap widening effect.

We then fabricated solar cell devices based on these new electron-extracting contacts. CQDs were synthesized and washed following reported methods (Experimental Section). Capacitance–voltage measurements were used to study the depletion width in these devices at the MPP (**Figure 3**a). As the In content is increased the capacitance decreases, attributable to the increased depletion of the CQD film.[27] The depletion width calculated from these studies (Figure S4, Supporting Information) reveals
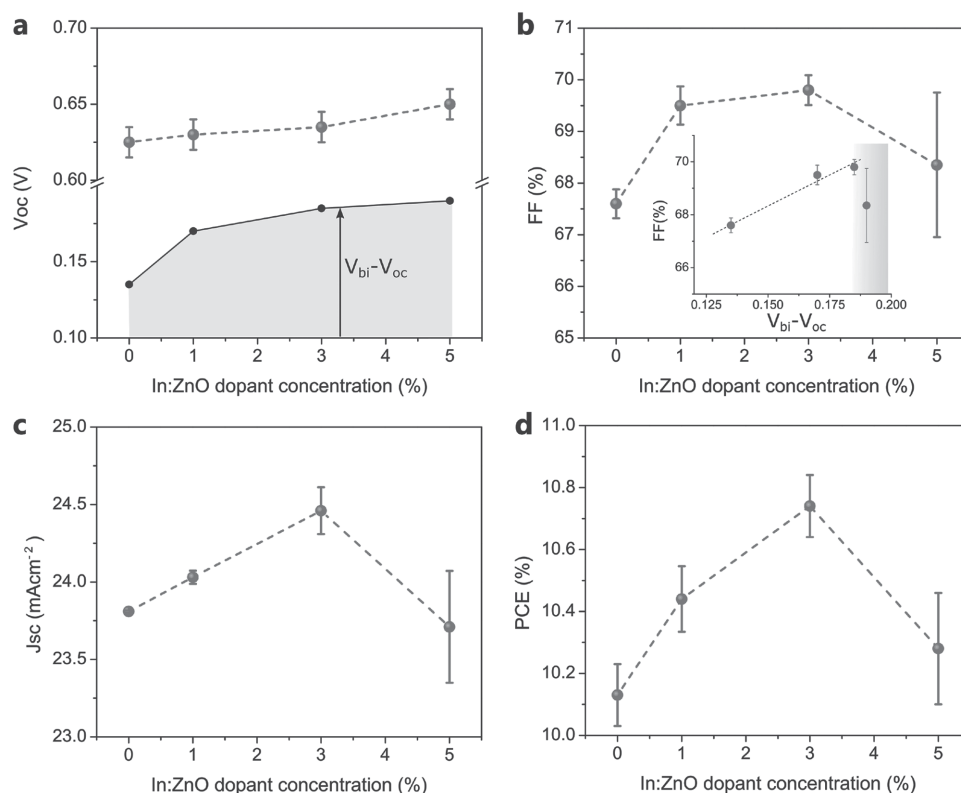

Figure 4. Photovoltaic figures of merit as a function of ZnO doping. a) Open-circuit voltage (V_{oc}) and ($V_{bi} - V_{oc}$) available potential (inset). b) Fill factor (FF) and its dependence with the potential budget (inset). c) Short-circuit current (J_{sc}) and d) PCE of CQD devices with ZnO substrates over a doping series measured under AM 1.5G illumination. Both current and FF are maximized as a result of enlarged depletion and quasi-neutral region minimization at maximum power point conditions (double-sided junction). A record PCE of 10.8% is obtained for 3% In:ZnO devices. Error bars represent the standard deviation calculated over the performance of at least ten different devices.

Materials
Views
www.MaterialsViews.com

ADVANCED
MATERIALS
www.advmat.de

COMMUNICATION

an increase of 80 nm for the highest doping, 5% In:ZnO. The combined drift+diffusion length is expected to reach 110 nm (diffusion) + 80 nm (drift), a 210 nm value that exceeds the film thickness (Figure 3b). This confirms our hypothesis that highly doped ZnO significantly extends the depletion width in CQD layer even at MPP. The built-in potential (V_{bi}) also increases desirably (Figure 3c and Figure S5, Supporting Information) due to the increased difference between the Fermi level of ZnO and of PbS.

Devices were prepared on both In-doped ZnO substrates and reference ZnO, and were tested under 100 mW cm^{-2} AM1.5G irradiation. V_{oc}, FF, J_{sc}, and PCE are plotted in **Figure 4**. Maximum performance is obtained for 3% In:doped ZnO, mainly due to the improvement in FF and short-circuit current, which increase, respectively, from 68% and 23.8 mA cm^{-2} to 70% and 24.3 mA cm^{-2}. This results in the highest PCE of 10.8%, notably superior to the PCE of 10.1% obtained for undoped control devices. We note that both control and doped devices retain their stability under ambient storage over the course of an initial 30 day study (Figure S6, Supporting Information).

The observed improvement in performance can be explained by the increased depletion width and built-in potential of the In:doped devices. In Figure 4a we plot the open-circuit voltage and V_{bi} excess ($V_{bi} - V_{oc}$) for the different concentrations. The remaining built-in potential helps sustain significant band bending even at maximum power point conditions. The reduced

recombination due to the diminished quasi-neutral region translates into the observed fill-factor increase (Figure 4b), the photovoltaic figure of merit in which the most striking improvements are obtained. Given the similar absorbances of devices with different ZnO substrates (Figure S7, Supporting Information), the higher J_{sc} is posited to arise from the more efficient charge extraction both in CQDs layer and at In:ZnO/PbS interface (increased W_D at 0 V). A diminution in J_{sc} and FF is seen at 5% dopant concentration, in agreement with simulated predictions for overdoped ZnO as well as with the possibility of increased defects that could reduce the mobility of free charges. The current density versus voltage characteristics of the representative control and double-sided junction devices under simulated AM1.5G illumination are shown in **Figure 5**a, and the photovoltaic figures of merit for the different In dopant concentrations are summarized in **Table 2**. The increased fill factor showcases the improved charge collection under positive voltages and together with increase in J_{sc} and V_{oc} leads to record 10.8% PCE (Figure 5b).

External quantum efficiency (EQE) spectra shown in Figure 5c confirm the better photocarrier extraction for double-sided junction devices at short-circuit conditions. This is especially the case for high-energy photon excitations, which, being absorbed in the vicinity of the ZnO–PbS interface, greatly benefit from increased depletion widths (Figure 1b). The calculated
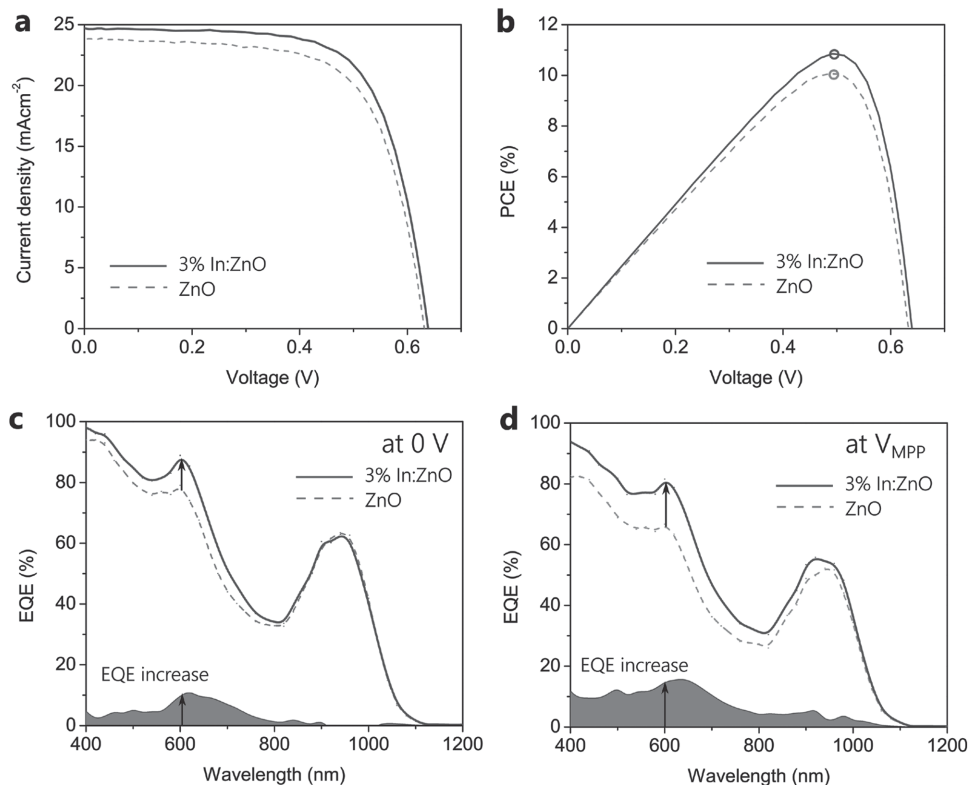

Figure 5. Current–voltage and spectral response of double-sided junction optimized devices. a) Current–voltage characteristics of control and 3% In-doped ZnO samples under simulated AM 1.5G illumination. A maximum 10.8% PCE is obtained. b) Power-conversion efficiency as a function of forward bias voltage and maximum power point. c) The external quantum efficiency at short-circuit conditions illustrates the CQD spectral contribution and the increase below 600 nm due to enhanced depletion. The calculated J_{sc} is 24.03 mA cm^{-2} for 3% In:ZnO versus 23 mA cm^{-2} for control ZnO, which is consistent with the measured J_{sc}. d) The benefit of the double-sided junction is more remarkable at maximum power point conditions, with up to a 10–15% extra EQE through the visible spectrum.

COMMUNICATION

Table 2. Device characteristics of CQD photovoltaics with different ZnO substrates.

	V_{oc} [V]	J_{sc} [mA cm^{-2}]	FF [%]	PCE [%]
Pure ZnO devices	0.63	23.81	67.63	10.1
1% In:ZnO devices	0.63	24.03	69.45	10.4
3% In:ZnO devices	0.64	24.32	69.84	10.8
5% In:ZnO devices	0.65	24.13	68.08	10.4

increase of 1 mA cm^{-2} in J_{sc} based on the spectral EQE is consistent with the one obtained under AM 1.5G illumination. The benefit of the double-sided junction is even more remarkable in Figure 5d, where we plot the EQE at MPP conditions for both control ZnO and 3% In:ZnO doped samples. Due to the additional electric field in the double-sided junction, an extra 10%–15% EQE is obtained across the visible spectrum, leading to a significant increase in J_{mpp} and FF.

In this work we report the successful implementation of a double-sided junction CQD PV architecture that leads to a record PCE of 10.8%. This is achieved by re-engineering the ZnO electrode using a solution-processable strategy. The incorporation of In^{3+} into ZnO results in a dramatic increase in carrier concentration up to 5×10^{19} cm^{-3}. As a consequence, a significant built-in electric field can be sustained even at maximum power point conditions at both the PbS-TBAI/PbS-EDT and PbS/In:ZnO rectifying interfaces. This results in minimized recombination and maximized fill factors. The increase in depletion width upon In incorporation further contributes to maximized J_{sc} and J_{mpp}, as the combination of drift and diffusion lengths surpasses the thickness of the photoactive CQD layer which translates into improved charge collection efficiency. A record PCE of 10.8% is achieved for In:doped double-sided junction devices, compared to a PCE of 10.1% for standard control devices. The presented double-sided junction strategy is compatible with the advantages of solution processable CQD photovoltaics, offering a direct approach to increase the PCE of CQD solar cells.

Experimental Section

CQD Synthesis and Solution Treatment: PbS CQDs were synthesized using previous methods.[8,10] The QD solution was pretreated by iodine, then washed and redispersed following reported recipe.[12]

In:ZnO Sol–Gel Preparation and Film Deposition: ZnO sol–gel synthesis was based on a modification of a previously reported method.[28] 0.1 M of zinc acetate dihydrate and monoethanolamine (1:1 molar ratio) were dissolved in 2-methoxyethanol solution. The mixture was stirred overnight at room temperature. The solution was filtered through a 0.2 µm filter and then deposited onto the ITO substrate by spin-coating at 3000 rpm for 30 s. The as-deposited film was then annealed at 200 °C for 10 min. For In-doped ZnO preparation, indium chloride is added in sol–gel solution.

Solar-Cell Fabrication: PbS QDs were deposited onto ZnO substrate using a layer-by-layer spin-casting process. For the TBAI-treated films, two drops of PbS CQDs in octane (50 mg mL^{-1}) were deposited and spin-cast at 2500 rpm. TBAI (10 mg mL^{-1}) in methanol solution was then applied to the film for 30 s, followed by a two-time methanol rinsing step. The process was repeated seven times. For two EDT-treated PbS layers, a 0.01 vol% EDT in acetonitrile solution was deposited to the film

for 30 s, followed by a three-time acetonitrile rinsing step. On top of the PbS QDs films, 120 nm Au was deposited as the top electrode through a shadow mask to define 0.053 cm^2 electrodes.

Device Characterization: J–V characterization: Current–voltage traces were acquired with a Keithley 2400 source measuring unit under simulated AM1.5G illumination (Sciencetech class A). The spectral mismatch was calibrated using a reference solar cell (Newport), yielding a correction multiplicative factor of $M = 0.848$. Devices were measured under a continuous flow of nitrogen gas. The source intensity was calibrated using a Melles–Griot broadband power meter and a Thorlabs broadband power meter through a circular 0.049 cm^2 aperture at the position of the device and also confirmed with a calibrated reference solar cell (Newport, Inc.).

Device Characterization: EQE Measurement: External-quantum-efficiency spectra were taken by subjecting the cells to monochromatic illumination (400W Xe lamp passing through a monochromator and appropriate cutoff filters). The output power was calibrated with Newport 818-UV and Newport 838-IR photodetectors. The beam was chopped at 220 Hz and focused in the pixel together with a solar-simulator at 1 sun intensity to provide for light bias. The response of the cell was acquired with a Lakeshore preamplifier connected to Stanford Research 830 lock-in amplifier at short-circuit conditions.

Device Characterization: Capacitance–Voltage Measurement: The capacitance–voltage measurements were acquired with an Agilent 4284A LCR meter at a frequency of 1 kHz and an AC signal of 50 mV, scanning from −1 V to 1 V. All measurements were performed in the dark.

Device Characterization: SCAPS: CQD photovoltaic devices were modeled with SCAPS simulation suite.[29,30] The parameter space and simulation details are available in Table S8 (Supporting Information).

Materials Characterization: XPS and UPS Measurement: XPS and UPS spectra of ZnO films are measured on Au substrate. Photoelectron spectroscopy was performed in a PHI5500 Multi-Technique system using monochromatic Al-K$_\alpha$ radiation (XPS) ($h\nu = 1486.7$ eV) and non-monochromatized He-I$_\alpha$ radiation (UPS) ($h\nu = 21.22$ eV). All work function and valence-band measurements were performed at a takeoff angle of 88°, and the chamber pressure was ≈10^{-9} Torr. Work functions (W_F) were calculated from the secondary electron cutoff (SEC) using equation $W_F = 21.22$ eV − SEC. The differences between Fermi levels and valence band maximum, η, were determined from the low binding energy onset.

Materials Characterization: UV–vis Absorption: Optical absorption measurements were carried out in a Lambda 950 500 UV–vis–IR spectrophotometer.

Materials Characterization: Calculation of the Carrier Concentration: The calculation of the doping concentration was based on the Joyce–Dixon model for degenerately doped semiconductors.[31] A conduction-band density of states of 4.4×19 cm^{-3} was assumed for the ZnO based on published data.[32]

Supporting Information

Supporting Information is available from the Wiley Online Library or from the author.

Acknowledgements

[1] V. M. Wood, J. Panzer, J. Chen, M. S. Bradley, J. E. Halpert, M. G. Bawendi, V. Bulović, *Adv. Mater.* **2009**, *21*, 2151.

[2] Q. J. Sun, Y. A. Wang, L. S. Li, D. Y. Wang, T. Zhu, C. H. Yang, Y. F. Li, *Nat. Photonics* **2007**, *1*, 717.

[3] K. Jeonghun, K. B. Wan, D. G. Lee, I. Park, J. Lim, M. Park, H. Cho, H. Woo, D. Y. Yoon, K. Char, S. Lee, C. Lee, *Nano Lett.* **2012**, *12*, 2362.

[4] G. Konstantatos, I. Howard, A. Fischer, S. Hoogland, J. Clifford, E. Klem, L. Levina, E. H. Sargent, *Nature* **2006**, *442*, 180.

[5] J.-S. Lee, M. V. Kovalenko, J. Huang, D. S. Chung, D. V. Talapin, *Nat. Nanotechnol.* **2011**, *6*, 348.

[6] S. Y. Jeong, S. C. Lim, D. J. Bae, Y. H. Lee, H. J. Shin, S.-M. Yoon, J. Y. Choi, O. H. Cha, M. S. Jeong, D. Perello, M. Yun, *Appl. Phys. Lett.* **2008**, *92*, 243103.

[7] S. Yang, N. Zhao, L. Zhang, H. Zhong, R. Liu, B. Zou, *Nanotechnology* **2012**, *23*, 255203.

[8] A. H. Ip, S. M. Thon, S. Hoogland, O. Voznyy, D. Zhitomirsky, R. Debnath, L. Levina, L. R. Rollny, G. H. Carey, A. Fischer, K. W. Kemp, I. J. Kramer, Z. Ning, A. J. Labelle, K. W. Chou, A. Amassian, E. H. Sargent, *Nat. Nanotechnol.* **2012**, *7*, 577.

[9] C.-H. M. Chuang, P. R. Brown, V. Bulović, M. G. Bawendi, *Nat. Mater.* **2014**, *13*, 796.

[10] Z. Ning, O. Voznyy, J. Pan, S. Hoogland, V. Adinolfi, J. Xu, M. Li, A. R. Kirmani, J. Sun, J. Minor, K. W. Kemp, H. Dong, L. Rollny, A. Labelle, G. Carey, B. Sutherland, I. Hill, A. Amassian, H. Liu, J. Tang, O. M. Bakr, E. H. Sargent, *Nat. Mater.* **2014**, *13*, 822.

[11] A. J. Labelle, S. M. Thon, S. Masala, M. M. Adachi, H. Dong, M. Farahani, A. H. Ip, A. Fratalocchi, E. H. Sargent, *Nano Lett.* **2015**, *15*, 1101.

[12] X. Lan, O. Voznyy, A. Kiani, F. P. García de Arquer, A. S. Abbas, G. H. Kim, M. Liu, Z. Yang, G. Walters, J. Xu, M. Yuan, Z. Ning, F. Fan, P. Kanjanaboos, I. J. Kramer, D. Zhitomirsky, P. Lee, A. Perelgut, S. Hoogland, E. H. Sargent, *Adv. Mater.* **2016**, *28*, 299.

[13] P. Guyot-Sionnest, *C. R. Phys.* **2008**, *9*, 777.

[14] J. Gao, J. M. Luther, O. E. Semonin, R. J. Ellingson, A. J. Nozik, M. C. Beard, *Nano Lett.* **2011**, *11*, 1002.

[15] A. H. Ip, A. Kiani, I. J. Kramer, O. Voznyy, H. F. Movahed, L. Levina, M. M. Adachi, S. Hoogland, E. H. Sargent, *ACS Nano* **2015**, *9*, 8833.

[16] M. M. Lee, J. Teuscher, T. Miyasaka, T. N. Murakami, H. J. Snaith, *Science* **2012**, *338*, 643.

[17] J. Tang, H. Liu, D. Zhitomirsky, S. Hoogland, X. Wang, M. Furukawa, L. Levina, E. H. Sargent, *Nano Lett.* **2012**, *12*, 4889.

[18] G. H. Carey, L. Levina, R. Comin, O. Voznyy, E. H. Sargent, *Adv. Mater.* **2015**, *27*, 3325.

[19] I. J. Kramer, D. Zhitomirsky, J. D. Bass, P. M. Rice, T. Topuria, L. Krupp, S. M. Thon, A. H. Ip, R. Debnath, H. Kim, E. H. Sargent, *Adv. Mater.* **2012**, *24*, 2315.

[20] National Center for Photovoltaics, http://www.nrel.gov/ncpv/; accessed: October 2015.

[21] A. G. Pattantyus-Abraham, I. J. Kramer, A. R. Barkhouse, X. Wang, G. Konstantatos, R. Debnath, L. Levina, I. Raabe, M. K. Nazeeruddin, M. Grätzel, E. H. Sargent. *ACS Nano* **2010**, *4*, 3374.

[22] D. Zhitomirsky, O. Voznyy, L. Levina, S. Hoogland, K. W. Kemp, A. H. Ip, S. M. Thon, E. H. Sargent, *Nat. Commun.* **2014**, *5*, 3803.

[23] P. Nunes, E. Fortunato, P. Tonello, F. Braz Fernandes, P. Vilarinho, R. Martins, *Vacuum* **2002**, *64*, 281.

[24] S. Pati, P. Banerji, S. B. Majumder, *RSC Adv.* **2015**, *5*, 61230.

[25] A. Sarkar, S. Ghosh, S. Chaudhuri, A. K. Pal, *Thin Solid Films* **1991**, *204*, 255.

[26] K. Ellmer, *J. Phys. D: Appl. Phys.* **2001**, *34*, 3097.

[27] J. P. Clifford, K. W. Johnston, L. Levina, E. H. Sargent, *Appl. Phys. Lett.* **2007**, *91*, 253117.

[28] L. K. Jagadamma, M. Abdelsamie, A. E. Labban, E. Aresu, G. O. Ngongang Ndjawa, D. H. Anjum, D. Cha, P. M. Beaujuge, A. Amassian, *J. Mater. Chem. A* **2014**, *2*, 13321.

[29] M. Burgelman, P. Nollet, S. Degrave, *Thin Solid Films* **2000**, *361*, 527.

[30] M. Burgelman, K. Decock, S. Khelifi, A. Abass, *Thin Solid Films* **2013**, *535*, 296.

[31] S. M. Sze, K. K. Ng, *Physics of Semiconductor Devices*, 3rd Ed., John Wiley & Sons, Inc., Hoboken, NJ, USA **2007**, Ch. 1.

[32] C. Maragliano, S. Lilliu, M. S. Dahlem, M. Chiesa, T. Souier, M. Stefancich, *Sci. Rep.* **2014**, *4*, 4203.